

Optimum Image Extraction and Phase Analysis for ESPI Measurements Under Environmental Disturbance

S. Arikawa¹ · K. Ashizawa² · K. Koga² · S. Yoneyama²

Received: 14 August 2015 / Accepted: 28 January 2016 / Published online: 16 February 2016
© Society for Experimental Mechanics 2016

Abstract We propose a new technique for electronic speckle pattern interferometry (ESPI) for measuring static deformation under environmental disturbances. In this technique, a number of laser speckle images of the initial and deformed states are captured, and images appropriate for making interference fringes are extracted using the optimum image extraction method. The phase of the interference fringe pattern is evaluated from the extracted images using a random phase-stepping method. In this study, translation amounts by random vibration are used as the phase stepping amounts. To validate the effectiveness of the proposed technique, an in-plane rotation of a flat plate and a strain distribution around a weld line of a compressor tank are measured. A compact speckle interferometer constructed on a tripod is used for the measurement. As a result, an interference fringe can be obtained, and the subsequent phase analysis can be performed under the proposed method without a vibration isolator. It is expected that ESPI measurements under environmental disturbance will be possible using the proposed technique.

Keywords Electronic speckle pattern interferometry · Phase stepping method · Deformation · Strain measurement · Disturbance

Introduction

Electronic speckle pattern interferometry (ESPI) [1–3] is an optical interferometric technique for studying the mechanical deformation of solids. Interferometric techniques are very sensitive, do not involve contact, and are applicable to whole-field measurements. Thus, ESPI has been widely applied to static deformation measurement [4–6], dynamic deformation measurement [7–9], vibration mode analysis [10–12], and nondestructive testing [13–15]. Moreover, shape measurement techniques [16, 17] and a hybrid technique [18] with the digital image correlation method [19, 20] have been researched.

In general, interferometric measurements are performed on vibration isolators because of their sensitivity. This problem has led to increased measurement system sizes and has impeded their application to various fields, such as the inspection of factories or plants. However, some techniques for time variation phenomena can be applied to measurements without vibration isolators. In interferometric measurements for such phenomena, phase analysis by conventional phase-stepping methods is difficult. Therefore, many phase analysis techniques for dynamic phenomena have been proposed. For example, instantaneous capture of multiple phase-stepped images by a special charge-coupled device (CCD) camera with a micro-polarizer array [21–24], and a technique called the subtraction-addition method [25, 26] without phase stepping have been proposed. In phase analyses using spatial information about interference fringes, some methods using Fourier or wavelet transforms have been proposed [27–29].

✉ S. Arikawa
arikawa@meiji.ac.jp

¹ Department of Mechanical Engineering Informatics, School of Science and Technology, Meiji University, 1-1-1 Higashimita, Tama-ku, Kawasaki, Kanagawa 214-8571, Japan

² Department of Mechanical Engineering, College of Science and Engineering, Aoyama Gakuin University, 5-10-1 Fuchinobe, Chuo-ku, Sagamihara, Kanagawa 252-5258, Japan

Furthermore, techniques using time series information at a single coordinate [7, 30, 31] and one-step phase analysis [32] using the spatiotemporal information have been developed. However, to obtain phase information, it is necessary for the exposure time to be sufficiently short compared to the phase fluctuation at the same moment. If the velocity of the object increases, the use of a high-power laser is needed to ensure that the light intensity captured by the camera is sufficiently high. This results in high costs and large measurement system sizes. To apply ESPI measurements in various fields, it is advantageous for the measurement system to be compact, functional without a vibration isolator, and capable of operating under environmental disturbances such as random vibrations.

Conversely, an optimum image extraction method [33] for static deformation measurements under disturbance has been proposed. By this method, optimal images for producing interference fringes are extracted from a large number of images captured at the initial and deformed states. The extraction is based on the evaluation of the speckle contrast on time series values. The merit of this method is that an ordinary camera and a laser can be used for measurements without a vibration isolator, and a compact interferometer can be constructed on a tripod. However, applications of general phase-stepping methods that require a state of rest for the stepping are difficult for phase analysis.

In this study, we propose a new technique for ESPI measurements of static deformations under environmental disturbances. According to this technique, numerous laser speckle images of the initial and deformed states are captured, and images that can make interference fringes are extracted using the optimum image extraction method. For phase analysis, a random phase-stepping method [34] is applied using the extracted optimal images. Translation amounts by random vibration are used as the phase stepping amounts. To verify the applicability of this phase analysis technique with optimal image extraction, a measurement of a quantitative in-plane rotation is performed under an environmental random vibration. Moreover, to validate the effectiveness of the proposed technique, a strain distribution around a weld line of a compressor tank, resulting from a rise in pressure, is measured without vibration isolators as an environmental random vibration comes from the floor. A compact speckle interferometer constructed on a tripod that includes a middle-power laser is used for the measurement. The result shows that the phase can be analyzed using the extracted optimal images. In the deformation measurement, strain distributions around the weld line of the compressor tank can be measured by the proposed technique. It is expected that ESPI measurements should be possible in various environments using the proposed technique.

Formation of Interference Fringes and Phase Analysis

Outline of ESPI

Figure 1(a) shows a typical setup of a dual-beam interferometer sensing in-plane displacement. Two expanded coherent laser beams separated from a single light source illuminate the rough surface of an object. The resulting laser speckle pattern is captured by a digital camera placed in front of the surface. Figure 1(b) shows a typical laser speckle pattern formed on the image plane of the camera by random reflections of the coherent laser beams from the rough surface. The average speckle size [1, 3] is given by

$$s = 2.44\lambda F \quad (1)$$

where λ is the wavelength of the laser and F is the F -number of the camera lens. Corresponding to the surface movement, the intensities of each speckle are modulated because of the interference of the beams. The interfered intensity I is written as

$$I = A_1 + B_1 \cos \varphi \quad (2)$$

where A_1 is the average intensity, B_1 is the modulation amplitude, and φ is the phase difference between the two beams. The interference fringe is obtained by subtraction of the

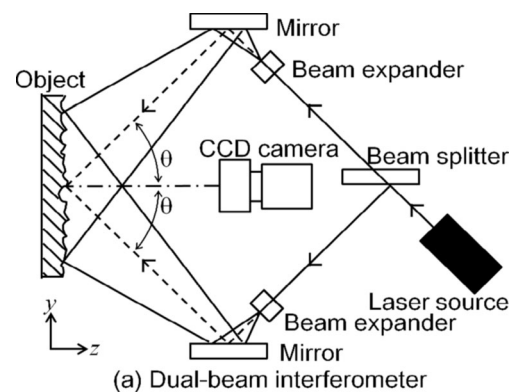


Fig. 1 Schematic of ESPI: (a) dual-beam interferometer, (b) typical resulting speckle pattern

deformed state image from the initial state image. The intensity, I_{sub} , of the subtracted image [1, 3] is calculated as

$$I_{\text{sub}} = |I_D - I_U| = \left| 2B_I \sin \left(\varphi_0 + \frac{\Delta\varphi}{2} \right) \sin \left(\frac{\Delta\varphi}{2} \right) \right| \quad (3)$$

where the subscripts U and D correspond to the initial and deformed states. φ_0 is the initial phase, and $\Delta\varphi$ is the phase difference of the deformed and initial states. The values of φ_0 at each point of the image are random, resulting in the high-frequency random noise seen in the random speckle pattern. However, the values of $\Delta\varphi$ result in the low-frequency fringe pattern due to surface deformation. The relationship between $\Delta\varphi$ and the displacement component u , which lies in the sensitive direction [1, 3], is given by

$$\Delta\varphi = \frac{4\pi u \sin \theta}{\lambda} \quad (4)$$

where θ is the incident angle of the beams, as shown in Fig. 1. Then, the displacement u_0 corresponding to one cycle (phase change of 2π) is

$$u_0 = \frac{\lambda}{2 \sin \theta} \quad (5)$$

The relationship between the displacement of one speckle and the sensing displacement is schematically drawn in Fig. 2. Each circle shows each state speckle position, and the hatched area shows the region where the speckles overlap. Here u_x and u_y are the displacement components along the x and y directions, respectively. As the calculable region, the overlap region carries information about the phase difference because image subtraction is performed at the same position in each of two state images. When the sensitive direction lies on the y -axis, only the y -component of the sensing displacement, u_y , is obtained from the information.

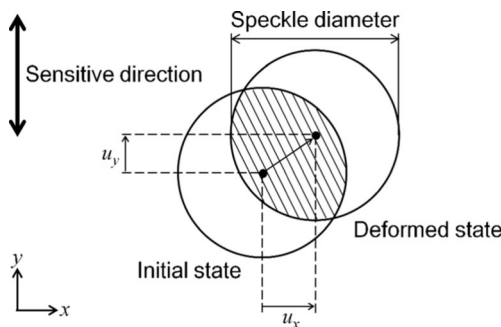


Fig. 2 Relationship between the displacement of one speckle and the sensing displacement

Optimal Image Extraction

If the profile of an instant vibration that comes from the floor is assumed to be a sinusoidal wave, the vibration displacement, u_v , at a point on an object as a function of time is

$$u_v = A_v + B_v \sin(\psi_0 + \omega t) \quad (6)$$

Where A_v is the average displacement of the vibration, B_v is its modulation amplitude, ψ_0 is its initial phase, and ω is its angular velocity. Taking into consideration the vibration profile given in equation (6), the intensity given in equation (2) can be rewritten as

$$I = A_I + B_I \cos \left[\varphi_0 + \frac{4\pi \sin \theta}{\lambda} \{A_v + B_v \sin(\psi_0 + \omega t)\} \right] \quad (7)$$

where φ_0 is the initial phase. Then, the average intensity captured over the exposure time, t_e , is

$$I_c = \frac{1}{t_e} \int_{t_e} \left(A_I + B_I \cos \left[\varphi_0 + \frac{4\pi \sin \theta}{\lambda} \{A_v + B_v \sin(\psi_0 + \omega t)\} \right] \right) dt \quad (8)$$

If B_v is sufficiently smaller than one cycle of displacement u_0 in equation (5), or if t_e is sufficiently smaller than $2\pi/\omega$, the unaveraged intensity value can be obtained. In general environments, it is difficult to employ such a condition without a vibration isolator. If B_v and t_e are large, the captured intensity, I_c , approaches the average intensity, A_I , and the phase information degrades. However, when the vibration phase of $(\psi_0 + \omega t)$ is a near multiple of π , the object velocity approaches zero. Therefore, I_c captured at such moments contains the phase information. This means that images captured at moments with sufficiently low velocity are optimal images for obtaining the interference fringes.

The optimum image extraction method [32] is based on the assumption that the dominant type of object motion caused by the disturbance is translation. The relationship between the disturbance as a random vibration and time are shown in Fig. 3(a). The curve shows the profile of a random vibration. The left-hand vertical axis gives the vibration displacement of a point on the surface, and the horizontal axis gives the time. The right-hand vertical axis represents the phase in equation (2) as the interfered intensity field, which is formed in the superimposed region of two beams on the object surface shown in Fig. 1(a). There are some high and low velocity moments.

The profiles of the intensity values during the exposure time t_e at moments of high and low velocity are considered. The relationship between the intensity and time interval at a high velocity moment is shown in Fig. 3(b). More than one cycle of intensity modulation occurs. Only the mean intensity

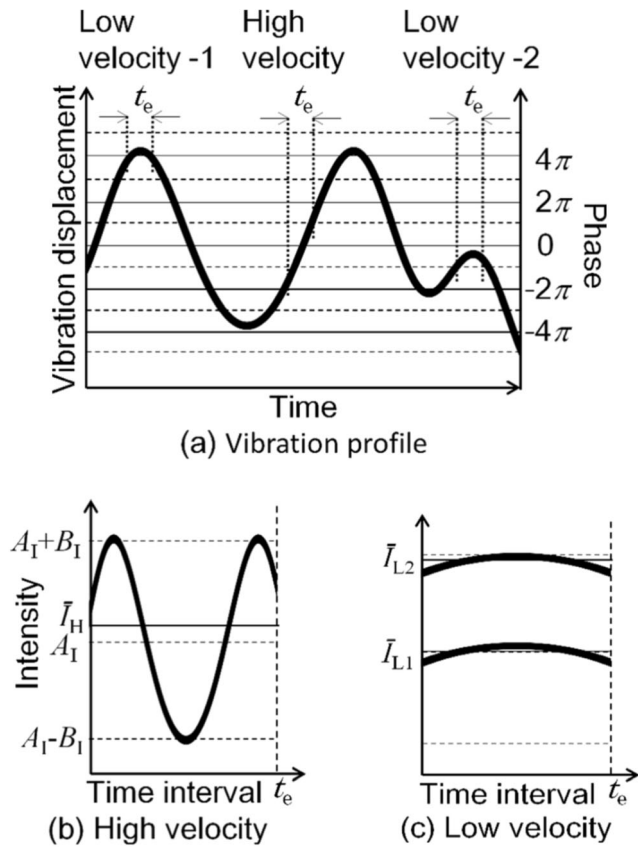


Fig. 3 Relationship between the vibration displacement, time, and phase: (a) vibration profile, (b) high-velocity intensity, and (c) low-velocity intensity

value is captured, and is obtained as \bar{I}_H . Here \bar{I}_H is almost the same as the average intensity A_1 in equation (2). Therefore, in such high-velocity moments, the captured intensities are always close to the average value, even if the displacement changes. In contrast, in the low velocity moments labeled “Low velocity-1” and “Low velocity-2” in Fig. 3(a), the captured intensities are not always close to the average because the changes in the intensity profiles are smaller than one cycle, as shown in Fig. 3(c). In the case of “Low velocity-1,” the captured intensity, \bar{I}_{L1} , is the same as A_1 . However, in the case of “Low velocity-2,” the captured intensity, \bar{I}_{L2} , is different from A_1 . This means that the velocities are not distinguished only by the intensity value at a single point, and it is therefore necessary to evaluate differences between the captured intensity values and the average value at many points in images captured at various moments. For some pixels in each image, the sum of the absolute deviations of the intensity around the time average multiplied by n , E_i are calculated as

$$E_i = \sum_{j=1}^n |I_{ij} - \bar{I}_j| \tag{9}$$

where i and j are the time series image index and pixel index of each image, respectively, I_{ij} is the intensity value of the image i

at pixel j , and \bar{I}_j is the time average value at pixel j . The largest resulting sum, E_{max} , indicates the optimal image. The evaluation stability increases with an increasing number of evaluation points, n . The required n number is investigated later in this paper.

Phase Analysis

Many phase analysis methods have been researched [7, 21–32, 34–37]. In this study, applications of subtraction-addition [25, 26] and random phase-stepping methods [34] are investigated. In the subtraction-addition method, the object is not required to be at a state of rest. The outline of the method is as follows. The phase difference, $\Delta\varphi$, is given as

$$\Delta\varphi = \tan^{-1} \left(\frac{\langle I_{sub} \rangle}{\langle I_{add} \rangle} \right) \tag{10}$$

where ‘ $\langle \rangle$ ’ indicates spatial averaging over a small region to remove the high frequency spatial noise. Then, I_{add} , the added intensity is given as

$$I_{add} = |I_D + I_U - 2A_1| = \left| 2B \cos \left(\varphi + \frac{\Delta\varphi}{2} \right) \cos \left(\frac{\Delta\varphi}{2} \right) \right| \tag{11}$$

where A_1 on each point is obtained by time-averaging, as with \bar{I}_j in equation (9). In the phase map obtained using this method, the positive and negative signs of the phase values are reversed at every interval of π .

The aim of the optimum image extraction method is to measure deformation as a displacement gradient and not to measure the translation amount of the object. In this situation, it is reasonable to assume that the translation amounts are equal to the phase-stepping amounts for the phase analysis using the random phase-stepping method [34]. When numerous speckle images are captured at both the initial and deformed states, the initial state intensities, I_{Uij} , and the deformed state intensities, I_{Dij} , are written as

$$I_{Uij} = A_j + B_j \cos(\varphi_{Uj} + \Delta\varphi_{vi}) \tag{12}$$

$$I_{Dij} = A_j + B_j \cos(\varphi_{Dj} + \Delta\varphi_{vi'}) \tag{13}$$

where the subscript v indicates components influenced by vibration, i and i' are the initial and deformed state time series image indices, respectively, $\Delta\varphi_{vi}$ and $\Delta\varphi_{vi'}$ are the phase difference components caused by the vibration of the initial and deformed states, respectively, and j is the pixel index that indicates the position in the image. Then, the relative displacement distribution, u_{vj} , is written as

$$u_{vj} = C(\varphi_{Uj} - \varphi_{Dj}) \tag{14}$$

where C is a sensitivity constant related to the laser

wavelength and the incident angle. The relative displacement, u_{ij} , includes an unknown translation amount caused by the vibration. However, differentiation of u_{ij} with respect to space gives us a deformation term, the strain ε_j , as

$$\varepsilon_j = \frac{d}{dx} u_{ij} \quad (15)$$

In these phase analysis methods, the mathematical sign cannot be distinguished. Accordingly, we have to choose a reasonable sign for the phase change. In this study, these phase analysis methods are applied, and their results are compared.

Validation of Phase Analysis

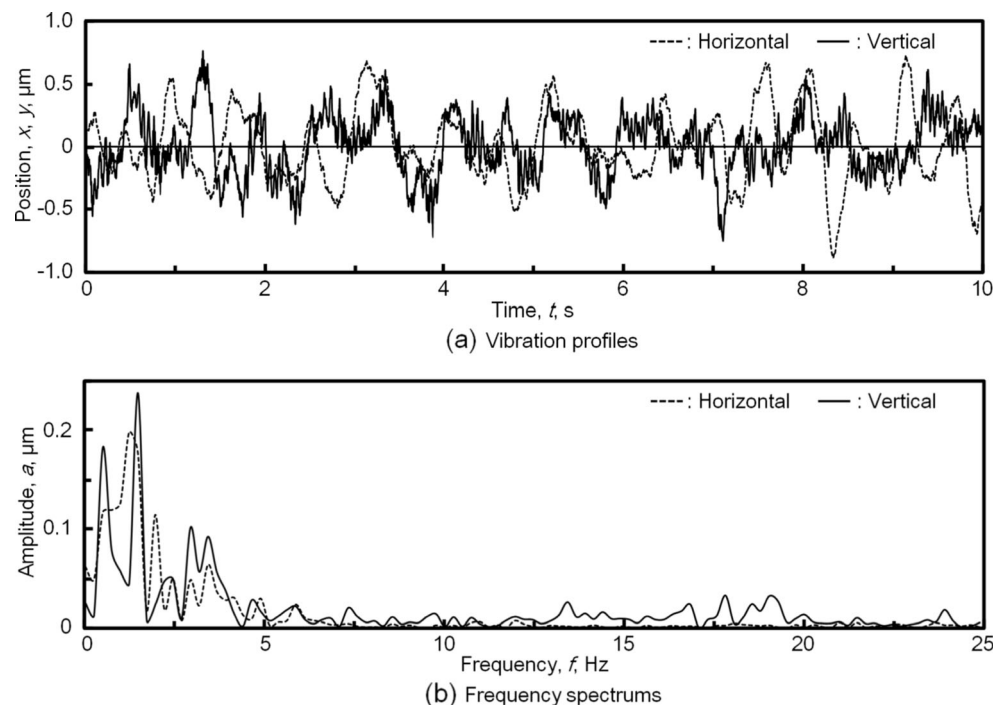
Experiment Setup and Procedure

For validation of the phase analysis, an experiment is performed under the environmental disturbance coming from the floor. The ESPI setup of a typical dual-beam interferometer is arranged to perform the vertical displacement measurement, as shown in Fig. 1(a). A 32 mW He–Ne laser (Melles Griot, Model 05-LHP-928) with a wavelength of 632.8 nm is used. The monochrome CCD camera (Sony, Model XCD-X710) has a resolution of 1024×768 pixels, a cell size of $4.65 \mu\text{m} \times 4.65 \mu\text{m}$, and a maximum frame rate of 30 frames/s. The laser beam is separated by a beam splitter and illuminates the object surface. The incident angle of the beams

is 45° . Then, the laser beams are expanded by beam expanders and illuminate a larger area. The F -number of the camera lens is set to 5.6. The exposure time is set to 10 ms. This is the shortest exposure time necessary to capture an image with sufficient intensity in this condition. The object is not connected with the ESPI setup. Hence, the relative position between the interferometer and the object is modulated by the environmental disturbance.

To obtain the details of the disturbance in the laboratory located on the second floor of the building, vibration displacements are measured using a vibration detector (Showa Sokki Corporation, Model 2205). The measured vibration profiles and the fast Fourier transform results are shown in Fig. 4(a) and (b), respectively. The profiles show that the amplitudes and the frequencies of the vibration are random. Moreover, in addition to the low-frequency components, the high-frequency components are detected in the vertical component of the vibration. The distance between the maximum and minimum positions is approximately $1.5 \mu\text{m}$. This distance is larger than the u_0 of 447 nm, which is the displacement corresponding to one cycle of the phase in this experimental condition. Therefore, when the exposure time for capturing the image is long, the captured intensity value approaches the average intensity. The average speckle size calculated by equation (1) is approximately $8.6 \mu\text{m}$ under the conditions of this study. This means that the overlapping region, indicated by the hatched region in Fig. 2, is easily obtained, and thus, the interference fringes can be made when optimal images are extracted from images recorded at sufficiently low-velocity

Fig. 4 Vibration analysis results: (a) vibration profiles, (b) frequency spectra



moments. In the frequency spectra, the major frequency components are distributed under 5 Hz. Additionally, some minor frequency components of the vertical vibration are distributed around 18 Hz. This suggests that if the exposure time is longer than 1/18 s, the quality of the captured phase information will degrade into vertical-sensing speckle images.

In the experiment, to investigate the phase analysis, a rigid body rotation measurement is performed on an aluminum plate. To perform phase analysis by the subtraction-addition method, the average intensity, A_i , in equations (2) and (11) is calculated from both speckle image states for all images. To obtain the phase value, the speckle images with the largest E_i values in each state are used. To perform phase analysis by the random phase-stepping method, four speckle images with the largest E_i values are used to calculate the phase, φ_j , for each state. The maps of the phase change, $\Delta\varphi$, obtained from each method are compared later on. Additionally, Phase-unwrapping is performed using the phase change map obtained with the random phase-stepping method.

Result and Discussion

Before the phase analysis, the optimal number of evaluation points indicated by n in equation (9), was investigated by evaluating the relationship between the dispersion of the evaluation values of the extraction and the number of evaluation points. For the evaluation, 100 speckle images were captured using the unidirectional measurement setup under environmental disturbance. The average evaluation values, E_i/n , were calculated from the captured speckle images. The evaluation points, n , were taken by a pitch longer than five pixels as discontinuous points on each speckle image. The pitch was longer than the average speckle diameter of 1.85 pixels (8.6 μm). When a large number of speckle images of one state were captured, the evaluation values, E_i/n , were obtained for each image. Then, the standard deviation, SD , of the dispersion of E_i/n was evaluated for various numbers, n . It is expected that SD should be high when there are not a sufficient number of evaluation points. To compare the results under various conditions, the standard deviation ratio SD' , the ratio of such as SD value to the largest value, is evaluated.

Examples of distributions of the average evaluation values, E_i/n , at the two conditions $n=500$ and 8000 are shown in Fig. 5(a). According to these results, the image with $i=93$ has a relatively high evaluation value, as shown in the figure. When $n=500$, the values are distributed around the value of 20, whereas when $n=8000$, the values are concentrated slightly higher than 20. The relationship of the standard deviation ratio, SD' , to the number of evaluation points, n , is shown in Fig. 5(b). The abscissa is n on a logarithmic scale. The results show that SD' decreases with increasing n . In the range of small n , SD' decreases drastically. In the range of large n , SD' converges to approximately 0.1. As the decrease of SD'

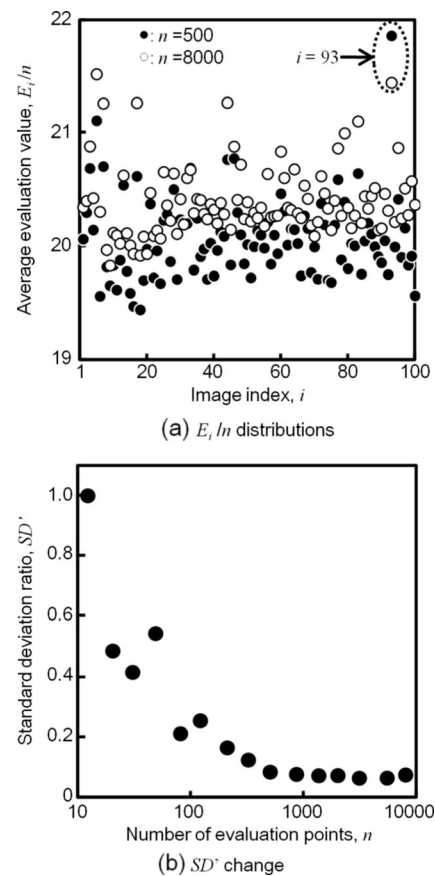


Fig. 5 Evaluation results: (a) distributions of average evaluation values, E_i/n , (b) relationship between standard deviation ratio, SD' , and number of evaluation points, n

is very small in the range of $n > 1000$, it is not necessary to use more than 1000 evaluation points for image extraction. In this study, the evaluation points are selected at discontinuous points with pitches longer than the average speckle size of the images. This means that 1000 speckles are evaluated. Usually, the values of the initial phases, φ , shown in equation (2) are random. This suggests that it is not necessary to use more than 1000 evaluation points representing speckles for image extraction, even if the experimental conditions are different from those in this study.

For the phase analysis, the in-plane rotation is measured. The given rotation angle is approximately 7.5×10^{-5} rad. 100 speckle images are captured for each of the rotated and initial states. Examples of the speckle images of each state are shown in Fig. 6(a) and (b). The rotation cannot be distinguished by the naked eye because the rotation angle is very small.

Optimal image extraction is undertaken for the speckle images of each state, and phase analyses are then performed. Figure 6(c) and (d) show the wrapped phase-change $\Delta\varphi$ maps obtained by the subtraction-addition and random phase-stepping methods, respectively. The phase map obtained by the subtraction-addition method looks like the fringe pattern

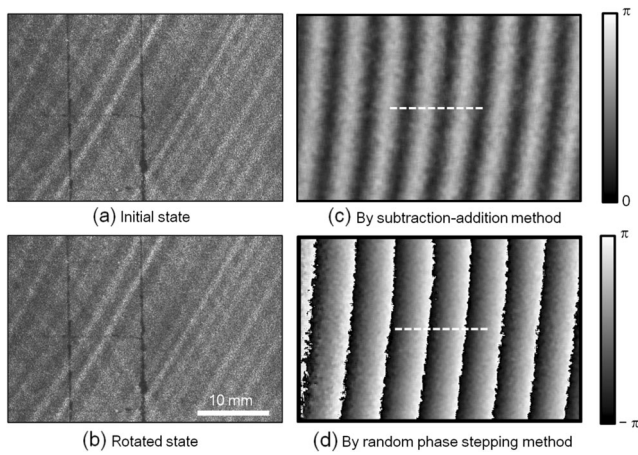


Fig. 6 Captured speckle images of the (a) initial and (b) rotated states; phase difference maps obtained by the (c) subtraction-addition and (d) random phase-stepping methods

of a subtracted image because the positive and negative signs of the $\Delta\varphi$ values are reversed at every interval. By this method, the peak lines of the phase change distribution are obscured because spatial averaging with a window size of 11×11 pixels is performed for the subtracted and added images. Conversely, the phase map obtained by the random phase-stepping method shows a comparatively good result in the ESPI measurement. In this analysis, the sign of the phase change is chosen on the basis of the given rotation direction. When in-plane rigid body rotation is observed by vertical sensing, the y -axis-sensing ESPI, $\partial\Delta\varphi/\partial x$ is proportional to the rotation angle of the object, and $\partial\Delta\varphi/\partial y$ is zero. In such cases, the fringe lines are parallel to the y -axis. Since the fringe lines in Fig. 6(c) and (d) are slightly distorted, it is expected that minor out-of-plane rotation around the x -axis occurs. The value of $\partial\Delta\varphi/\partial y$ is calculated to be roughly $\pi/25$ rad/mm and has a displacement gradient of approximately 9×10^{-6} . This value causes error in the measurement. The error ratio is 12 % of the given angle, even though the given angle is very small. The error ratio will decrease with an increase in the given angle, because the error is independent of this angle. Therefore, it is expected that deformation measurements are possible by the proposed technique.

Wrapped phase-change $\Delta\varphi$ profiles along the dashed lines on each $\Delta\varphi$ map are shown in Fig. 7. The region of the values obtained by the subtraction-addition method is $0 \leq \Delta\varphi \leq \pi$, because these values are obtained from the inverse tangent using absolute values, as shown in equations (3), (10), and (11). However, the upper and lower peaks are obscured. To obtain an accurate phase change distribution using this method, investigations of the spatial filtering and unwrapping processes are required. Conversely, the values obtained by the random phase-stepping method range from $-\pi$ to π and are easy to use in phase unwrapping, although the sign cannot be distinguished. In this case, a reasonable sign of the phase change is chosen according to the given rotation.

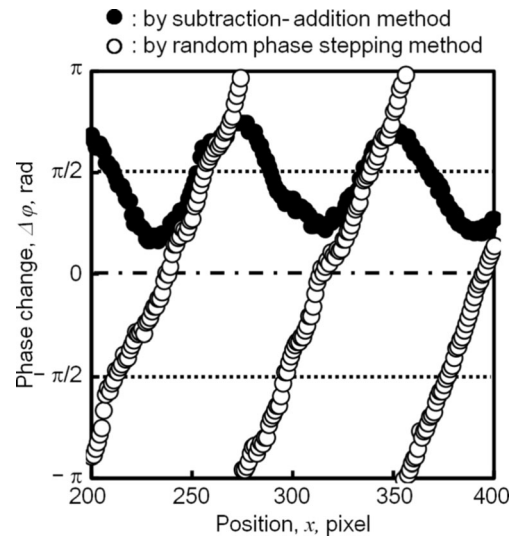


Fig. 7 Phase-difference profiles obtained using each method along the white dashed lines shown in Fig. 6

The unwrapped phase change map obtained from the wrapped phase in Fig. 6(d) is shown in Fig. 8(a). The phase-change distribution indicating vertical displacement shows a constant gradient. The displacement distribution is obtained from the unwrapped phase change. The profile of the displacement corresponding to the white dashed line is shown in

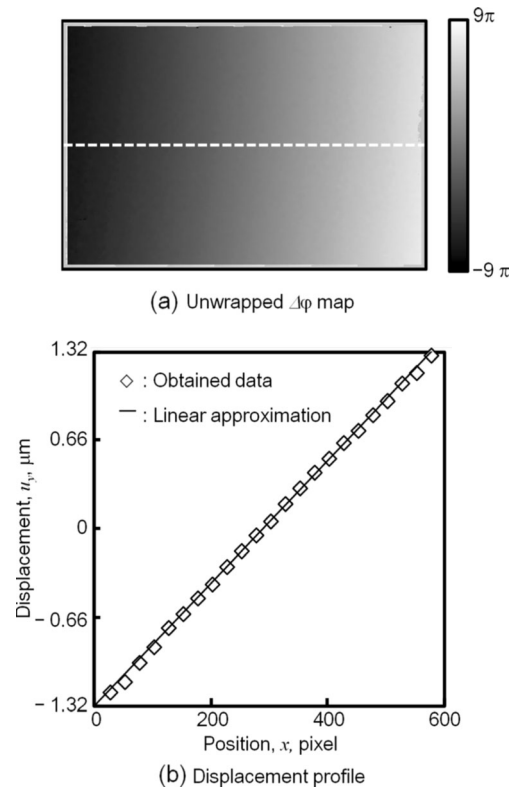


Fig. 8 Analysis results of (a) the unwrapped $\Delta\varphi$ map obtained from the phase using the random phase-stepping method, and (b) the displacement profile obtained by the local least squares approach along the white dashed line

Fig. 8(b). The ordinate is the vertical displacement, u_y . The white diamonds indicate the displacements obtained by phase analysis, and the line indicates the linear approximation. The standard deviation of the error between the measured values and the linear approximation is 27 nm, and the maximum absolute error is 97 nm. The maximum error ratio is 3.7 %, compared with the total measurement range of 2.64 μm . Additionally, the R^2 value is 0.999. The results show very good linearity. The rotation angle calculated from the linear approximation is 7.16×10^{-5} rad, which agrees well with the given angle. The error ratio is about 4.5 % of the given value; therefore, the random phase-stepping method is effective for this technique, and static deformation measurements using optimal image extraction in ESPI under environmental disturbances are possible.

Deformation Measurement of a Compressor Tank

Experimental Setup and Procedure

The deformation around the weld line of a compressor tank is measured to demonstrate the effectiveness of the proposed technique. In this study, simultaneous bidirectional displacement measurement is performed using the proposed technique with the bidirectional optical setup reported by Moore et al. [38]. A schematic of the bidirectional measurement setup is shown in Fig. 9. Each of the two beams illuminates an observation region from the horizontal x - and vertical y -axes. Then, beam expanders are used on each laser beam, and they illuminate the large area. For bidirectional measurement with simultaneous image capturing in each direction, the polarizations of the laser beams for each sensitive direction are arranged orthogonally. A polarizing-beam splitter is set in front of the cameras to separate each polarization component of the laser beams with horizontal and vertical sensitivities. The CCD camera arrangement angle is approximately 45° because of the arrangement space in the compact interferometer. The incident angles of the laser beams are set to 11° for each direction. A constant-wave 300 mW diode-pumped solid state

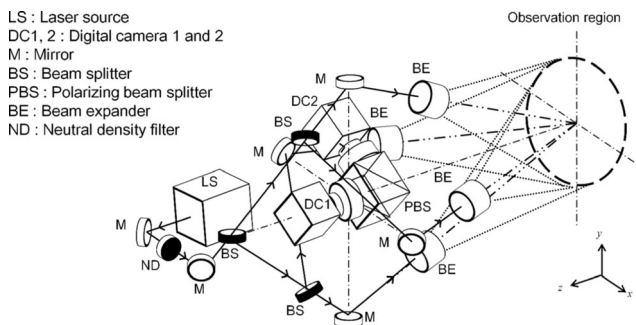
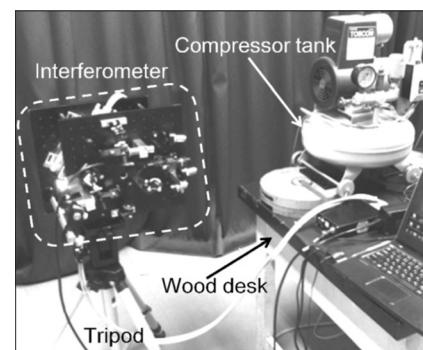
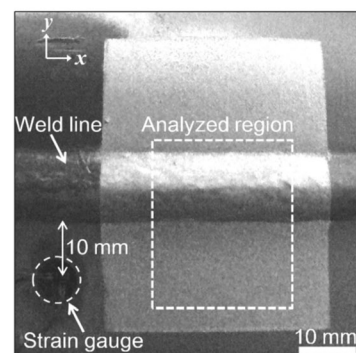


Fig. 9 Schematic of a compact interferometer for bidirectional measurement

(DPSS) laser (Klatsch, Scherzo) with a wavelength of 532 nm is used. The laser power is adjusted by a neutral density (ND) filter. The monochrome CCD cameras (Allied Vision Technologies, Guppy Pro F125B) each have a resolution of 1292×964 pixels, a cell size of $3.75 \mu\text{m} \times 3.75 \mu\text{m}$, and a maximum frame rate of 31 frames/s. The F -number of the camera lens is set to 4. The exposure time is set to 1.7 ms. Figure 10(a) shows the experimental setup. The compressor including the welded tank, is put on a wooden desk without vibration isolators. The interferometer attached to the tripod is set in front of the compressor tank. In this experimental condition, the disturbance is expected to be harder than that of the previous condition, because both the object and the interferometer are not isolated from the disturbance. Thus, the exposure time is set to six times shorter than that of the previous condition. Figure 10(b) shows the surface around the weld line of the tank. Aluminum powder is painted on the observation region to optimize the diffuse reflection and to reduce the disarrangement of the polarizations of the reflected laser beams. Aluminum powder with a particle size of less than $74 \mu\text{m}$ is adhered on the surface using a conventional stick spray. The analyzed region is indicated by the white dashed line. For reference, the biaxial strain gauge, which is arranged to measure ϵ_x and ϵ_y , is attached to the surface at a position 10 mm lower than the weld line. The deformation of the tank is measured when the pressure increases from 0.1 MPa to 0.6 MPa.



(a) Experimental setup



(b) Observation region

Fig. 10 Views of (a) experimental setup and (b) observation region

The data processing flow for deformation measurement is as follows. First, numerous images for both the horizontal and vertical sensitivities at both the initial and deformed states are captured. Second, the optimal images for each image set are extracted. Third, the phase-stepping method is applied for phase analysis. Finally, the strain distributions are calculated by the local least-squares method. By this process, strain maps for each component can be obtained.

Results and Discussion

Examples of captured speckle images are shown in Fig. 11(a) and (b). The image size is 500×600 pixels, and the length of the region shown in a pixel is approximately $62 \mu\text{m}$. Intensities on the border of the weld line are relatively dark because of the curvature of the weld surface. The phase analysis is performed using extracted speckle images for each state and direction. The results are shown in Fig. 11(c) and (d). In this case, reasonable signs of the phase changes are decided by the measurement results of the strain gauge. Additionally, a spatial filtering region size of 21×21 pixels is used to remove some noise from the analyzed results. The phase change distribution of the vertical sensitivity is larger than that of the horizontal sensitivity. The phase distribution around the center of the vertical sensitive phase map is slightly disordered. It is

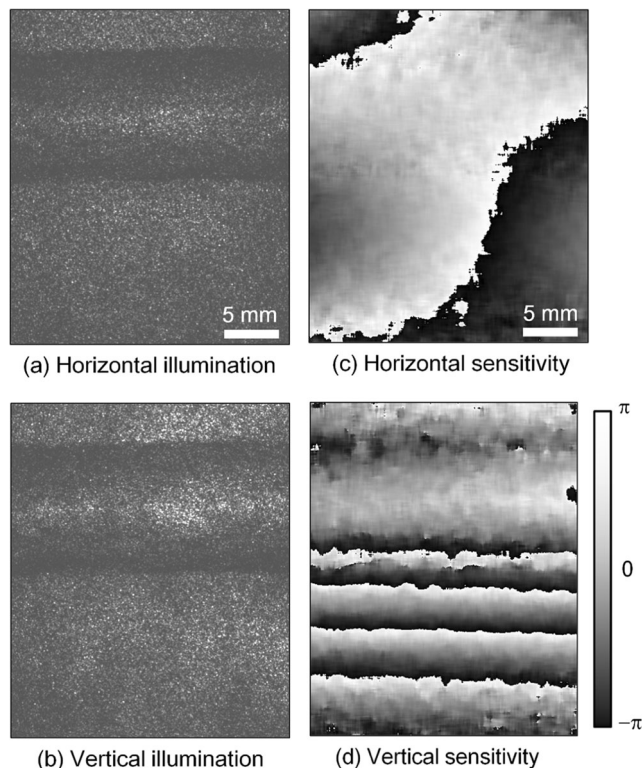


Fig. 11 Captured speckle images for each sensitive illumination: (a) horizontal illumination, (b) vertical illumination; wrapped $\Delta\varphi$ maps obtained by a random phase-stepping method for each direction: (c) horizontally sensitive $\Delta\varphi$ map, (d) vertically sensitive $\Delta\varphi$ map

expected that the intensity of the border of the weld line is not sufficient for phase analysis.

Strain analyses are performed for the phase change maps using the local least-squares method with a calculation area of 21×21 pixels. The obtained strain components, ε_x , ε_y , and γ_{xy} , are shown in Fig. 12(a), (b), and (c). In the ε_x map, strain values are relatively low and constant. In the ε_y map, a slightly disordered region along the border of the weld line is observed. However, the overall strain distribution can be obtained. High strain values are observed on the lower side, and strain values drastically change on the weld line. The strain distribution is unsymmetrical across the weld line. It is believed that this strain distribution occurs because the tank shape is also unsymmetrical across the weld line. In the γ_{xy} map, shear strain values show values near zero. The white dashed lines are located at the same distance as the strain gauge from the weld line. The average strain values along the dashed lines are 3.7×10^{-5} for ε_x and 2.81×10^{-4} for ε_y . Strain values from the strain gauge are 2.7×10^{-5} for ε_x and 2.91×10^{-4} for ε_y . The error is $\pm 1 \times 10^{-5}$. Therefore, relatively good results were obtained.

The above results validate that bidirectional displacement measurements by ESPI under the environmental disturbance are possible. To apply this technique in other environments, such as industrial areas or plants, the amplitude of the environmental vibration and the displacement of the object during deformation should be considered, because the measurable limit is affected by such displacements. However, if the displacement is larger than the limit, ESPI measurements under

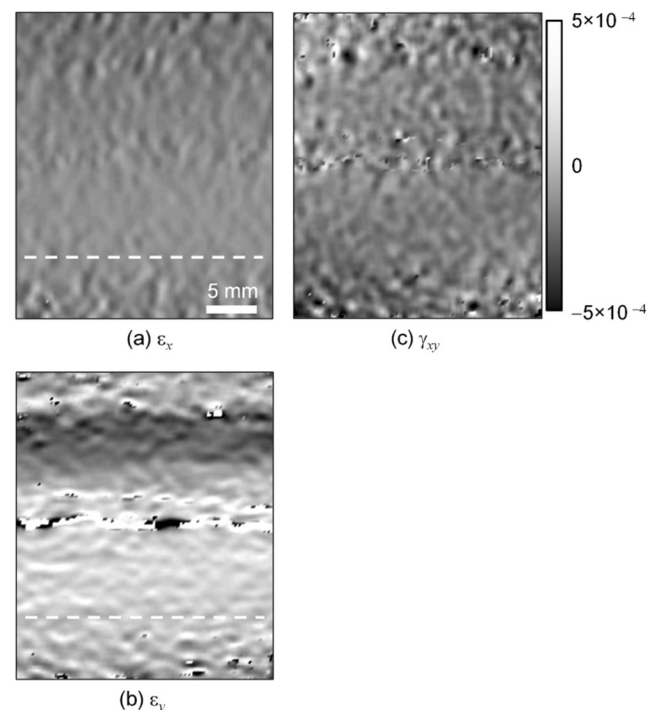


Fig. 12 Strain distributions around the weld line: (a) ε_x map, (b) ε_y map, and (c) γ_{xy} map

the proposed technique are still possible by applying a position correction to the speckle pattern [39–41]. In this case, a marker that can track the surface motion must be placed on the object's surface to apply a digital image correlation method [19, 20]. Incidentally, the sign of the phase analyzed by the random phase-stepping method must be decided. In many cases, the sign can be determined on the basis of the given conditions. If the sign cannot be determined, an additional measurement such as a strain measurement by a strain gauge at a point on the object surface is required. However, solving such problems is not difficult. Therefore, it is expected that ESPI measurements in various environments are possible using the proposed technique.

Conclusion

A new technique for ESPI measurements of static deformations under environmental disturbances is proposed. According to this technique, numerous laser speckle images of the initial and deformed states are captured, and images that can be used to make interference fringes are then extracted using the optimum image extraction method. The phase of the interference fringe pattern is analyzed from the extracted images using a random phase-stepping method. Translation amounts by random vibration are used as the phase stepping amounts. To validate the effectiveness of the proposed technique, an in-plane rotation of a flat plate and the strain distribution around the weld line of a compressor tank, resulting from an increase in pressure, are measured. A compact speckle interferometer constructed on a tripod that includes a middle-power laser is used to obtain the measurements. Using this method, an interference fringe can be obtained, and the phase can be analyzed without a vibration isolator. Additionally, the strain distribution around the weld line of a compressor tank can be measured using the proposed technique. The obtained strain measurement error of $\pm 1 \times 10^{-5}$ is very small. Therefore, it is expected that ESPI measurements in various environments are possible using the proposed technique.

Acknowledgments This work was supported by Japan Society for the Promotion of Science, Grant-in-Aid for Young Scientists (B), Grant Number 25870699.

References

- Jones R, Wykes C (1983) Holographic and speckle interferometry. Cambridge University Press, Cambridge
- Chiang FP (1989) Speckle metrology, ASM handbook volume 17, Nondestructive Evaluation and Quality Control 432–437, ASM International
- Sirohi RS (2002) Speckle interferometry. *Contemp Phys* 43(3): 161–180
- Vial-Edwards C, Lira I, Martinez A, Münzenmayer M (2001) Electronic speckle pattern interferometry analysis of tensile test of semihard copper sheets. *Exp Mech* 41(1):58–62
- Hinsch KD, Gülker G, Kelmers H (2007) Checkup for aging artwork—optical tools to monitor mechanical behavior. *Opt Lasers Eng* 45:578–588
- Arikawa S, Yoneyama S (2011) A simple method for detecting a plastic deformation region formed by local loading using electronic speckle pattern interferometry (in Japanese). *Trans Jap Soc Mech Eng, Ser A* 77(775):383–390
- Madjarova V, Kadono H, Toyooka S (2003) Dynamic Electronic Speckle Pattern Interferometry (DESPI) phase analyses with temporal Hilbert transform. *Opt Express* 11:617–623
- Ikeda T, Ichinose K, Gomi K, Yoshida S (2007) Study of dynamic fracture toughness measuring method by electronic speckle pattern interferometry (in Japanese). *Proc Mech Eng Congress 2011, Jap Soc Mech Eng* 7-1:57–58
- Arikawa S, Gaffney JA, Gomi K, Ichinose K, Ikeda T, Mita T, Rourks RL, Schneider C, Yoshida S (2007) Application of electronic speckle pattern interferometry to high-speed phenomena. *J Mater Test Res Assoc Jap* 52(3):176–184
- Ma C, Huang C (1998) Vibration characteristics for piezoelectric cylinders using amplitude-fluctuation electronic speckle pattern interferometry. *AIAA J* 36(12):2262–2268
- Chen C, Huang C, Chen Y (2009) Vibration analysis and measurement for Piezoceramic rectangular plates in resonance. *J Sound Vib* 326:251–262
- Huang Y, Ma C (2009) Experimental and numerical investigations of vibration characteristics for parallel-type and series-type triple-layered Piezoceramic bimorphs. *IEEE Trans Ultrason Ferroelect Freq Control* 56(12):2598–2611
- Silva Gomes JF, Monteiro JM, Vaz MAP (2000) NDI of interface in coating systems using digital interferometry. *Mech Mater* 32:837–843
- Gryzagoridis J, Findeis D, Tait RB (2005) Residual stress determination and defect detection using electronic speckle pattern interferometry. *Insight - Non-Destruct Test Condition Monitor* 47(2): 91–94
- Ambu R, Aymerich F, Ginesu F, Priolo O (2006) Assessment of NDT interferometric techniques for impact damage detection in composite laminates. *Compos Sci Technol* 66:199–205
- Parra-Michel J, Martínez A, Anguiano-Morales A, Rayas JA (2010) Measuring object shape by using in-plane electronic speckle pattern interferometry with divergent illumination. *Meas Sci Technol* 21:1–8
- Genovese K, Lamberti L, Pappalettere C (2004) A comprehensive ESPI based system for combined measurement of shape and deformation of electronic components. *Opt Lasers Eng* 42:543–562
- Arikawa S, Tominaga Y, Yoneyama S (2011) Speckle interferometry-digital image correlation hybrid method for wide range strain measurement (in Japanese). *J Jap Soc Experiment Mech* 12(3):235–242
- Bruck HY, McNeill SR, Sutton MA, Peters WH (1989) Digital image correlation using Newton-Raphson method of partial differential correction. *Exp Mech* 29(3):261–268
- Yoneyama S (2010) Displacement and strain measurement using digital image correlation (in Japanese). *J Jap Soc Non-Destruct Inspect* 59(7):306–310
- Yoneyama S, Sakaue K, Kikuta H, Takashi M (2006) Instantaneous phase-stepping photoelasticity for the study of crack growth behavior in a quenched thin glass plate. *Meas Sci Technol* 17:3309–3316
- Yoneyama S, Kamihoriuchi H (2009) A method for evaluating full-field stress components from a single image in interferometric photoelasticity. *Measure Sci Technol* 20. doi:10.1088/0957-0233/20/7/075302, (8pp)



23. Tahara T, Ito K, Kakue T, Fujii M, Shimozato Y, Awatsuji Y, Nishio K, Ura S, Kubota T, Matoba O (2010) Parallel phase-shifting digital holographic microscopy. *Biomed Optics Express* 1(2):610–616
24. Yoneyama S, Arikawa S (2014) Micro-polarizer array based instantaneous phase-stepping interferometry for observing dynamic phenomena. *Conf Proc Soc Experiment Mech Ser* 2014 3:229–233, **Springer**
25. Yoshida S, Suprapedi, Widiastuti R, Triastuti ET, Kusnowo A (1995) Phase evaluation for electronic speckle-pattern interferometry deformation analyses. *Opt Lett* 20:755–757
26. Madjarova V, Toyooka S, Widiastuti R, Kadono H (2002) Dynamic ESPI with subtraction-addition method for obtaining the phase. *Opt Commun* 212:35–43
27. Takeda M, Ina H, Kobayashi S (1982) Fourier-transform method of fringe-pattern analysis for computer-based topography and interferometry. *J Opt Soc Am* 72(1):156–160
28. Ma J, Wang Z, Vo M, Luu L (2011) Parameter discretization in Two-dimensional continuous wavelet transform for fast fringe pattern analysis. *Appl Opt* 50(34):6399–6408
29. Yoneyama S, Arikawa S, Kugiyama Y (2012) Interference and photoelastic fringe pattern analysis using snapshot imaging polarimetry. *J Jap Soc Experiment Mech* 12(Special Issue):s157–s162
30. Servin M, Davila A, Quiroga SA (2002) Extended-range temporal electronic speckle pattern interferometry. *Appl Opt* 41(22):4541–4547
31. Equis S, Jacquot P (2008) Phase extraction in dynamic speckle interferometry with empirical mode decomposition and Hilbert transform. *Strain*. doi:10.1111/j.1475-1305.2008.00451.x (9pp)
32. Bruno L, Poggialini A (2008) Phase shifting speckle interferometry for dynamic phenomena. *Opt Express* 16(7):4665–4670
33. Arikawa S, Nakaya Y, Yoneyama S (2012) Electronic speckle pattern interferometry with optimum image extraction for deformation measurement under environmental disturbance. *J Solid Mech Mater Eng* 6(6):634–644
34. Wang Z, Han B (2004) Advanced iterative algorithm for phase extraction of randomly phase-shifted interferograms. *Opt Lett* 29(14):1671–1673
35. Huntley JM (1998) Automated fringe pattern analysis in experimental mechanics: a review. *J Strain Anal Eng Des* 33(2):105–125
36. Kao CC, Yeh GB, Lee SS, Lee CK, Yang CS, Wu KC (2002) Phase-shifting algorithms for electronic speckle pattern interferometry. *Appl Opt* 41(1):46–54
37. Huang MJ, Yun B (2007) Self-marking phase-stepping Electronic Speckle Pattern Interferometry (ESPI) for determining a phase map with least residues. *Opt Laser Technol* 39:136–148
38. Moore AJ, Tyrer JR (1996) Two-dimensional strain measurement with ESPI. *Opt Lasers Eng* 24:381–402
39. Bingleman LW, Schajer GS (2011) DIC-based surface motion correction for ESPI measurements. *Exp Mech* 68:1207–1216
40. Arikawa S, Yoneyama S (2011) Correcting the effect of rigid body displacement in speckle interferometry (in Japanese). *J Jap Soc Experiment Mech* 11(3):195–200
41. Arikawa S, Yoneyama S (2013) Pattern position correction for measuring large deformation in speckle interferometry. *J Solid Mech Mater Eng* 7(3):417–425